Final Technical Report

DE-SC0005359

Assessing Regional Scale Variability in Extreme Value Statistics Under Altered Climate Scenarios

Reporting Period: 9/1/2010-8/31/2014
Funding Period: 9/1/2010-8/31/2014

PI: Nathaniel A. Brunsell, Department of Geography, University of Kansas
Co-PI: David B. Mechem, Department of Geography, University of Kansas
Co-PI: Chunsheng Ma, Department of Math and Statistics, Wichita State University

Project Synopsis:

One impact of anthropogenic climate change is an increase in extreme weather and climate events, which carry profound implications for drought, heat waves, and food production. These extreme climate events are modulated by low-frequency modes of atmosphere/ocean variability like the El Niño/Southern Oscillation (ENSO), the Pacific decadal oscillation (PDO), and the Atlantic multidecadal oscillation (AMO). Global climate models (GCMs) resolve these low-frequency modes with varying degrees of success, but the extreme events themselves are fundamentally realized on a local or regional level. Current GCMs may represent some aspects of these extreme weather and climate events, but because of the scale mismatch, the GCM realizations of these events are incomplete. Regional climate models can complete the picture by providing the focused level of local detail missing in the GCM output.

The goal of our project has been to evaluate the behavior of extreme weather events in the historical observational dataset, large-scale GCM simulations of 20th- and 21st-century climate, and suites of regional climate simulations driven by GCM output. This project has examined observational data and climate simulation output conducted over the continental United States by applying a recently developed technique that combines wavelet multi–resolution analysis with information theory metrics. This research is motivated by the following two fundamental questions concerning the spatial and temporal structure of extreme events:

1) What are the temporal scales of the extreme value distributions most sensitive to alteration by low-frequency climate forcings?
2) What is the nature of the spatial structure of variation in these timescales?

The primary objective was to assess how information theory metrics can be useful in characterizing the nature of extreme weather phenomena. Specifically, we have (1) addressed how changes in the nature of extreme events impact the temporal probability density functions, and the degree to which information theory metrics are sensitive these changes, and (2) characterized, via a wavelet multi–resolution analysis, the relative contribution of different timescales on the stochastic nature of extreme events.

This project has employed a unique combination of an established regional climate modeling approach and advanced statistical techniques to assess the effects of low-frequency modes on climate extremes over North America. Partway through the project, we transitioned from using the AR4 GCM output to that from the AR5 runs, the rationale being that the AR5 simulations better represented the low-frequency variability of interest and more realistically reflected possible 21st-century climate scenarios. The behavior of climate extremes in RCM simulations for the 20th century has been compared to historical climate from the North American Regional Reanalysis (NARR), the

United States Historical Climatology Network (USHCN), and simulations from the North American Regional Climate Change Assessment Program (NARCCAP). Our efforts serve to establish the baseline behavior of climate extremes, the validity of an innovative multi–resolution information theory approach, and the ability of the RCM modeling framework to represent the low-frequency modulation of extreme climate events.

Analysis of 20th century meteorological station data

We have focused on conducting an analysis of historical station observations as a baseline for comparison. The station data comes from the United States Historical Climate Network (USHCN, Menne et al. 2011) and the distribution is shown in figure 1. We have calculated the linear trends in the magnitude of extreme precipitation, daily maximum and minimum temperatures at the 90th, 95th, and 99th percentiles for both the intensity value and the number of exceedances. These values are all calculated on a per station basis and tested for statistical significance using the Mann-Kendall and other measures. These seasonal results were mapped to show the geographic coherence of both the magnitudes and the trends in the extreme events over the 20th century, as well as illustrating locations where extreme values are trending in opposite directions (e.g. southwestern US) (figures 2-7).

Of particular interest is the spatial and temporal (monthly/seasonal) variability in these trends. In an effort to aggregate the trends into meaningful biophysical and climatic units, we have chosen to use the Koeppen climate classification. Here, we have chosen to pursue only 9 of the 14 climates, as these climates account for over 95% of the land area in the U.S. This allows easy quantification of the geographic variability of the trends in relation to local climate. Through this aggregation, we are also looking at how the mean and the distribution of monthly slopes of extreme events (e.g. the 90th percentile precipitation intensity) vary across climatic regions and by month (Figures 9-10).

In addition, we have focused on 20th-century trends in extreme events by examining the changes in the distribution of extreme magnitude precipitation, minimum and maximum temperature for the 1950-1980 and the 1980-2009 periods (Figure 11). A paired t-test was performed on the data with the null hypothesis being there is no difference between the two samples. The samples that reject the null hypothesis with 95% confidence are indicated by an asterisk. For precipitation extremes, the climate groups that are non-stationary are BWh, BWk and Csa. The climate zones BWh, BWk and Csa all show trends for extremes in maximum temperature. All regions exhibit non-stationarity for extremes in minimum temperature, indicating that the distribution of cold extremes is changing. These trends are indicative of a shifting climate, resulting in a new distribution of extreme events for the future.

Multiscale decomposition and relationship between extreme events and regional teleconnection indices

Following the above analysis, we were able to quantify the nature of the extreme value distributions across the continental United States. The next stage of the project was to relate the variations in extreme value distributions to phases of the low-frequency modes of ENSO and PDO (Figure 12). We conducted a multiscale wavelet approach. Figure 13 shows the continuous wavelet transform for the normal versus extreme weather events and is averaged across Koeppen-Geiger climates. These results indicate that extreme events occur at different wavelet powers than normal daily events.

An example result is shown in Figure 13, which shows the wavelet co-spectra and coherency signal for precipitation and the ENSO in Lawrence, KS. This analysis was conducted for all 958 stations and spatially aggregated across climate zone.

For this study, an extreme event was quantified as an event that occurs above the 90th percentile of its monthly bin. There is a monthly bin for each month and the total number of months in each bin is based on the length of record. The monthly threshold values were calculated based on the previous analysis and are found to be unique for each station. This methodology provides a date for each extreme weather event and can be used for assessing normal weather events against those of extreme responses.

Geophysical time series can often exhibit non-stationarity, contain dominant periodic signals and hidden patterns. These time series can be decomposed using wavelets into signals, that vary in both time and frequency space. Long-term weather data can exhibit this periodic behavior as well as long-term climate patterns such as ENSO and PDO. Wavelet analysis allows the weather time series and the teleconnection signals to be analyzed at different periods throughout the length of the signal. They also provide the ability to simultaneously view the spatial and temporal nature of an extreme weather event against those of a normal weather event. For this study all wavelet transforms (continuous wavelet transform (cwt), wavelet cross wavelet transform (xwt) and wavelet transform coherence (wtc)) were conducted using the Biwavelet package (Gouhier and Grinsted, 2013) in R. Wavelet transform is chosen over Fourier transform due to the frequency localization limitation with Fourier transforms. Wavelets analysis avoids this issue by simultaneously decomposing in time space and frequency space. This allows for information regarding the power of any periodic signal as well as how that power varies over time.

These localized responses are taken separately for each extreme day and normal day and then averaged across each period to provide a final solution for a single localized response over time. An example of this process is shown for Station Number 011084 (Brewton, Al) in Figure 15 (a), where 15a shows the wavelet transform, 15b illustrated the time series highlighting the extremes and 15c provides detailed information about each probability density function (pdf) for the extreme and normal series and the average response for each scale. This process was completed for each station and then averaged across the 9 KG regions.

To ascertain the change in the relative influence of SOI and PDO signals on the extreme events to the normal, the xwt and wtc power spectrums were calculated and averaged for extreme days and normal days across each climate zone (an example is found in Figure 16). The example plot shows the xwt and wtc results for the decompositions of precipitation and SOI in Brewton, Alabama. The xwt and wtc plots are shown with the precipitation time series and the SOI signal. The extreme against those of a normal signal is not shown but follows the same process for averaging in time and is shown in Figure 16. This process was also completed for each station and then averaged across the 9 KG regions the same as described above. Both xwt and wtc were calculated for precipitation, maximum temperature, minimum temperature, SOI and PDO timeseries.

The average cwt decomposition for extreme and normal events within each KG zone are shown in Figure 17. Precipitation is column 1 (17a, 17b and 17c), maximum temperature is column 2 (17d, 17e and 17f) and minimum temperature is the last column (17g, 17h and 17i). The extreme spectra are shown as a dashed line where the normal spectra is a solid line. Scales that show a significant difference between the extreme and normal are shown with an asterisk and are significant at a p-value ≤ 0.05. Each time series was decomposed using a cwt at each USHCN station, and then averaged across 9 KG regions and grouped into 3 zones (Arid, Warm Temperate and Snow).

Following the analysis above, we were able to relate extreme events with regional climate teleconnections ENSO and PDO. The average arid, warm temperate and snow zone wtc(ppt,soi) decompositions are shown in Figure 18, column 1(18a, 18b and 18c). Figure 18d, 18e and 18f show the same but for wtc(ppt, pdo).

For wtc(ppt,pdo) the arid zone indicates that BSk and BWh have significantly different responses for extreme precipitation at 128 days and 512 days (BSk) and 256 days for BWh. The warm temperate zone shows that Cfa and Csb indicate significant differences within the periods of 32-512 days. Where the snow zone indicates later scales for significance at 128-512 for both Dfa and Dfb with an additional scale at 32 days for Dfb. High coherency is found with a peak at the annual timescale, which illustrates that the annual signal of precipitation is correlated with both teleconnections.

For the wtc(ppt, soi) the arid zone contains significantly different scales within the BSk at 32-256, the BWh at 64 and the BWK region at 64 and 256 days. The warm temperate zone shows significant scales within the Cfa region at 32-1024 days, and not so many for Csa and Csb at 64 and 32-256 days, respectively. For the snow zone the significance can be found in for Dfa and Dfb at 32-256 days or a period of 512 days, respectively. One difference is that the instead of high coherency at the annual the ppt, soi shows the opposite trend than ppt, pdo.

Overall, extreme weather events behave differently than normal events on specific timescales within different climate zones. The cwt results indicate that extreme precipitation separates from the normal at less than annual timescales. For maximum temperature, both extreme and normal events contain significant signals at the monthly timescale. For minimum temperature there are not many significant results in terms of the difference in extreme and normal responses. A significant difference is seen in the snow zone, which indicates extreme cold events vary in a different power spectra than normal.

The xwt results are indicative of phase differences and similarities between the time series and teleconnection patterns. Precipitation and SOI interactions are mostly significant at all scales while precipitation and PDO are only significantly different below the annual timescale. As both teleconnection patterns and precipitation spectra results move through time they become more in phase with each other, which indicates the precipitation has a high power spectrum which is significant on longer timescales, indicative of ENSO and PDO. In terms of xwt, results for temperature both maximum and minimum temperate exhibit similar results. Both peaking in phase consistency around the annual timescale, indicating that the annual temperature cycle is a dominate feature. In terms of separating normal from extreme events, this occurs in the longer timescales, and only within a few regions, indicating the sensitive nature of ENSO and PDO on temperature events.

The wtc results show how correlated two decompositions are, in this case extreme weather and either SOI or PDO. For all three extreme weather events there is an opposing peak of high correlation at the annual timescale for all the PDO transforms and a peak of low correlation between all the SOI transforms. The warm temperate zone shows many significantly different scales for precipitation while for temperature the majority of the differences can be found in the snow zone. This indicates there is more variability in warm temperature extreme precipitation and the role teleconnections play while the snow zone is most sensitive to temperature and teleconnection interactions.

Dynamical downscaling of extreme events

Our methodology consists of dynamically downscaling GCM simulations via a regional climate model (RCM). This effort has involved two approaches. First, we have explored the extreme value behavior for a subset of the simulations in the North American Regional Climate Change Assessment Program (NARCCAP; Mearns et al. 2009) model output. NARCCAP is a suite of simulations composed of a number of regional models driven by different GCMs. Figure 19 shows differences between 20th- and 21st-century for the 95th percentile of the distribution of daily precipitation. We deliberately selected runs with different driving GCMs to maximize the differences between models, and indeed the models diverge substantially in their projection of differences between precipitation extremes. The WRFG simulation shows strong increases in precipitation extremes over the southern plains; HRM3 and CRCM simulations exhibit weaker increases, and the ECP2 runs show little change. Simulation results over the desert southwest differ substantially: WRFG exhibits weaker extremes over the desert southwest, but ECP2 and HRM3 indicate stronger extremes. Most of the differences in extreme values are greater than changes to the central tendencies (medians). Therefore, the changes to the extrema stem from broadening of the distributions.

Probability distributions in the vicinity of three cities in widely different climate regimes (Fig. 20) sheds additional light on the behavior of precipitation extremes. The inter-model differences are especially apparent on this figure. For example, the CRCM model produces very little in the way of high-magnitude precipitation events. The 21st-century WRFG results over Nashville show a substantially increased distribution tail, which is consistent with the increase in 95th-percentile magnitude seen in Fig. 19.

Our longer-term modeling effort has revolved around conducting multi-decadal simulations in order to capture sufficient statistical realizations of the low-frequency modes (ENSO and PDO). Although we originally proposed simulations driven with CCSM3 GCM output, the substantial improvement of the representation of low-frequency modes of variability such as ENSO and PDO in CESM1/CCSM4 (Deser et al. 2012) caused us to reevaluate our efforts and begin to use CESM1 to drive our RCM simulations.

Our RCM simulations employ the Advanced Regional WRF (WRF v3.6), using initial and boundary conditions from CESM1. These simulations were a result of extensive collaboration with Andrew Monaghan at the National Center for Atmospheric Research (NCAR), who has substantial experience downscaling WRF with different versions of CCSM. WRF simulations of the periods 1950–1999 (beginning with CESM1 simulation b40.20th.track1.1deg.012) and 2050–2099 (RCP6.0 scenario) have been performed. Improved simulations currently underway cover the period from 1950–2061 and will eventually cover the entire

1950–2099 period. Our methodologies developed for analyzing the observational, GCM, and NARCCAP products have been applied to these long-term RCM simulations. We compare the variation in extreme events between driving model (CESM1) and regional model (WRF), and between 20th- and 21st-century simulations.

In our dynamical downscaling configuration, biases may arise from both the GCM and the RCM components. Model evaluation therefore becomes especially important to establish the veracity of any dynamical downscaling approach. The evaluation of NARCCAP output compared mean precipitation and temperature fields between the model results and the reanalysis data sets in order to quantify simulation bias (Mearns et al., 2012a; Bukovsky et al., 2013). In this research, we have evaluated the CESM-WRF downscaling approach by comparing long-term means of precipitation and temperature between every two members of these three data sets: WRF and CESM; WRF and NARR; NARR and CESM. Data from these three data sets are all chosen from the overlapping period of NARR and WRF, the years of 1979-1999. Figure 21 presents the difference maps for PR, TMAX, and TMIN, between WRF and CESM (WRF minus CESM), CESM and NARR (CESM minus NARR), as well as WRF and NARR (WRF minus NARR). This approach allows us to investigate the origin of the bias between CESM–WRF and the observational fields (as represented by NARR).

For precipitation, the region east of Mississippi River shows good agreement between WRF and NARR (< 125 mm annual difference). However, over the western mountainous U.S., the WRF-CESM simulation exhibits a substantial wet biase (Fig. 21a). Figure 21g suggests that WRF contributes substantially to the wet bias over the high topography and also appears to introduce a dry bias just downstream (east) of the mountain peaks. Both WRF and the driving CESM model exhibit the well-known dry bias. The greatest dry bias is over the southern states adjacent to the Gulf of Mexico, and then decreases towards the north (Fig. 21d).

We apply a bias correction using the linear scaling method (Lenderink et al., 2007), a relatively simple approach compared to other methods that rescale the entire distribution (Teutschbein and Seibert, 2012). This linear bias correction rescales the distribution such that the long-term mean of simulated distribution and the mean of observed distribution are equal. This method artificially rescales modeled PDFs to fit the observational (NARR) long-term means, but the distribution retains the same shape as the uncorrected PDFs. The long-term mean of PR is calculated from NARR over the interval 1979–1999.

Using the 90%, 95%, and 99% thresholds of the TMAX, TMIN, and PR distributions is one way we quantify extremes, and differences in these thresholds between 21st- and 20th-century simulations represent a trend in extreme events. For precipitation, the threshold differences increase for increasing percentiles (Fig. 22a, d, and g). The highest threshold differences are found over the south-central U.S. and southeastern U.S. near the Gulf Coast. Precipitation threshold differences increase from 3 mm in the 90% extreme map (Fig. 22a) to over 15 mm in the 99% extreme map (Fig. 22g). The increasing differences in precipitation for increasing threshold percentages suggests that the rarer the event, the greater (i.e., more extreme) will be the difference between projected and historical values. Similar TMAX threshold difference patterns across the different percentiles indicate that differences vary little as percentile increases (Fig. 22b, e, and h). Thresholds of the projected simulation are ~3-6 K higher than those of the historical simulation and vary widely over the whole domain. The greatest difference occurs over the north central U.S., just west of the Great Lakes, with a massive area of differences > 5 K for all three thresholds. TMIN threshold difference patterns are also largely similar across the different percentiles, although the magnitudes of the differences are greater than the increases in TMAX. This behavior is consistent with a reduction of the diurnal temperature variation in the projected simulation relative to the historical simulation.

In summary, systematic higher extreme percentile thresholds are found in PR, TMAX, and TMIN in the projected simulation, indicating that daily precipitation and daily maximum temperature are more extreme in the projected simulation, whereas daily minimum temperature behavior is less extreme (cold nights become warmer). For the TMAX and TMIN, substantial changes to TMIN thresholds appear more prevalent, a result consistent with lower projected diurnal temperature variation.

In order to quantify the behavior of extreme weather and climate events to the low-frequency modes of variability, we have conditionally sampled the simulation results by ENSO phase. ENSO conditions are classified as El Niño (warm phase), La Niña (cool phase), or neutral conditions by applying the southern oscillation index (SOI), calculated from the parent CESM1 output. We have found that the dependence of precipitation extremes on ENSO phase exhibits substantial geographic dependence, with large differences in the Pacific Northwest but smaller differences over the southeast.

In order to gain additional insight into the behavior of the extreme value statistics previously calculated, we aggregate the statistics across climate zones. We employ the Köppen-Geiger climate classification to divide the entire domain into 12 climate zones.

Figure 23 shows the springtime frequency and intensity of extreme precipitation distributions for spring (MAM). The box plots show both the historical (red) and projected (blue) simulation distributions. Colored dots over the median lines of some boxes indicate the statistical significance of differences between samples from the historical and projected simulations. We employ the two-sample student's t-test to evaluate statistical significance. Although the samples do not strictly fit to normal distribution, the sample sizes are sufficiently large (> 30) that the t-test is justified. The null hypothesis is that there is no difference between samples of the historical simulation and projected simulation (alpha = 0.05). The B class zones, which represent arid climatologies, have the lowest frequency and intensity medians. C class zones, which represent warm and humid climatologies, have higher frequency medians than B class zones but lower frequency medians than D class zones, and also the highest intensity medians (30-40 mm/event). D class zones that represent cold and snowy winter climatologies have frequency medians > 0.05 events/day and intensity medians slightly below 30 mm/event. Within the C class zones, Csa frequency and intensity behave differently compared to Cfa and Cfb. The different behavior of the Csa is largely a function of its coastal location but also may partly be a nonphysical result of the high precipitation bias over the mountainous west.

In nearly all zones, intensity in the projected simulation is greater than the respective historical value, and for most zones frequency is higher, too (BWk, BWh and Csa being the only zones with lower projected frequency). The four zones of Cfa, Cfb, Dfa, Dfb, which together includes most of U.S. east of the Rocky Mountains, have frequency and intensity differences that are tested significant.

In order to fully understanding the causes of the more extreme TMAX events and more heat waves with longer durations, in this section we plot the PDFs of TMAX for each climate zone in both the historical and projected simulations, and we calculated the difference of mean percentile values based on the historical and the projected simulations. PDFs are presented as violin plots in Fig. 24a. The 81st and 97.5th percentile values, as well as mean TMAX, are indicated by lines on the distributions. Difference of these percentile values, as well as the means for each climate zone are presented in Fig. 24b.

For the two thresholds used to quantify heat waves, the 97.5th percentile value determines how warm each heat wave is, while the 81st percentile value determines how many consecutive days can be included in a heat wave events. Therefore the heat wave frequency and duration are more profoundly affected by the 81st percentile value. Over most of the contiguous U.S. other than northeast, the mean TMAX increase in projected simulation is larger than the increase of the 81th percentile TMAX value. Considering the TMAX PDFs, other than the shifting of the whole distribution toward warmer side (increase of mean TMAX), there also higher percentage of days in the PDF higher than the mean TMAX in the projected simulation than in the historical simulation. As a result, the increase of mean TMAX is the predominate cause of more heat waves with longer durations in the projected simulation.

References

Bukovsky, M. S., D. J. Gochis, and L. O. Mearns, 2013: Towards assessing narccap regional climate model credibility for the north american monsoon: Current climate simulations*. *Journal of Climate*, 26 (22), 8802–8826.

Deser, Clara, and Coauthors, 2012: ENSO and Pacific Decadal Variability in the Community Climate System Model Version 4. *J. Climate*, **25**, 2622–2651.

Lenderink, G., A. Buishand, and W. v. Deursen, 2007: Estimates of future discharges of the river rhine using two scenario methodologies: direct versus delta approach. *Hydrology and Earth System Sciences*, 11 (3), 1145–1159.

Mearns, L. O., W. J. Gutowski, R. Jones, L.-Y. Leung, S. McGinnis, A. M. B. Nunes, and Y. Qian: A regional climate change assessment program for North America. *EOS*, Vol. 90, No. 36, 8 September 2009, pp. 311-312.

Teutschbein, C. and J. Seibert, 2012: Bias correction of regional climate model simulations for hydrological climate-change impact studies: Review and evaluation of different methods. *Journal of Hydrology*, 456, 12–29.

Figures

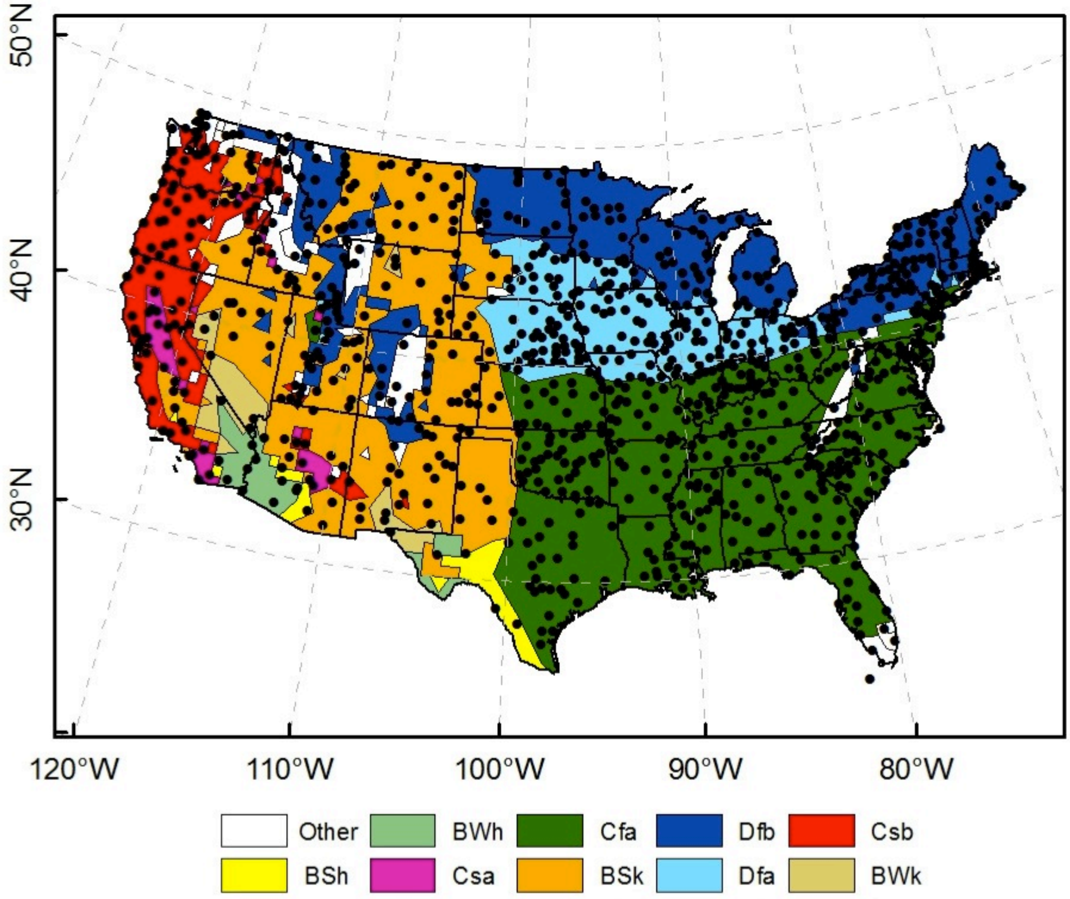

Figure 1. USHCN station distribution with corresponding Koeppen-Geiger classification.

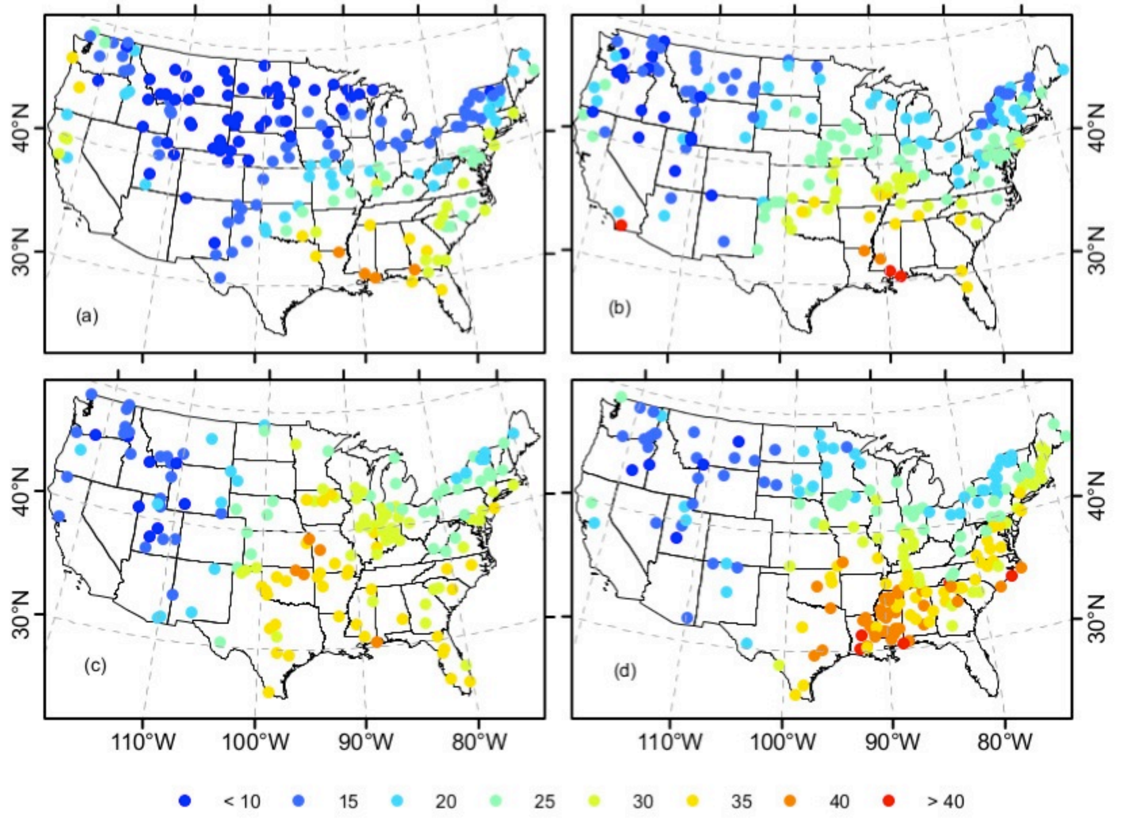

Figure 2. Magnitude threshold for an extreme precipitation event to occur [mm]. (a) Winter (178 significant stations), (b) Spring (171 significant stations), (c) Summer (156 significant stations) and (d) Fall (202 significant stations). Significant stations indicated by a Mann- Kendall p-value ≤ 0.05.

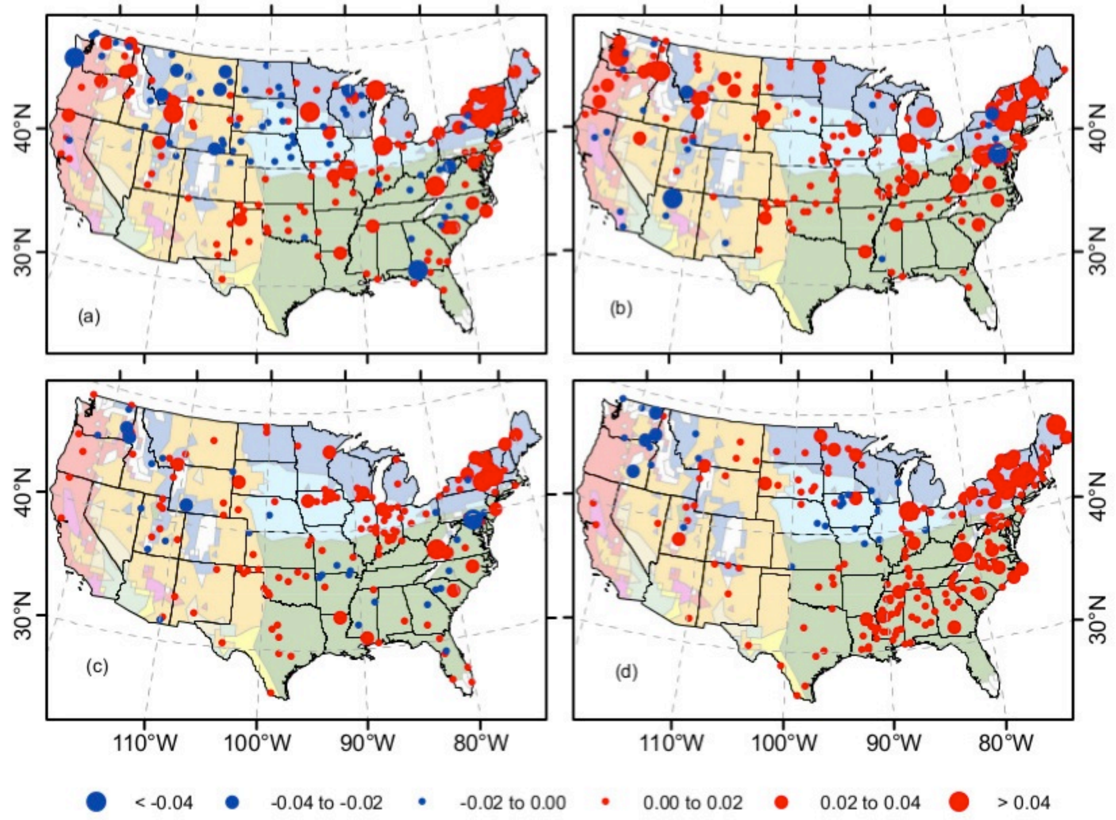

Figure 3. Slope of extreme precipitation events [number of extremes/year]. (a) Winter (178 significant stations), (b) Spring (171 significant stations), (c) Summer (156 significant stations) and (d) Fall (202 significant stations). Significant stations indicated by a Mann-Kendall p-value ≤ 0.05. Koeppen-Geiger classification are shown faded in bottom layer.

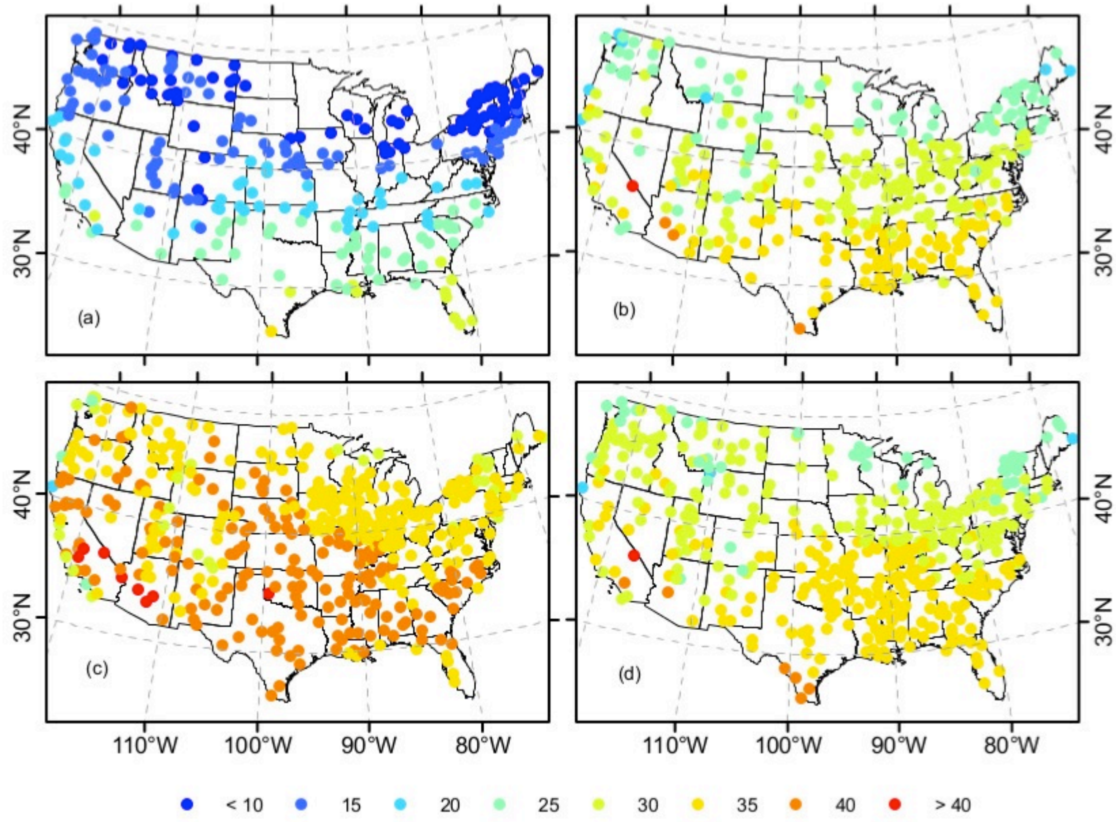

Figure 4. Magnitude threshold for an extreme maximum temperature event to occur [◦C]. (a) Winter (206 significant stations), (b) Spring (263 significant stations), (c) Summer (376 significant stations) and (d) Fall (362 significant stations). Significant stations indicated by a Mann-Kendall p-value ≤ 0.05.

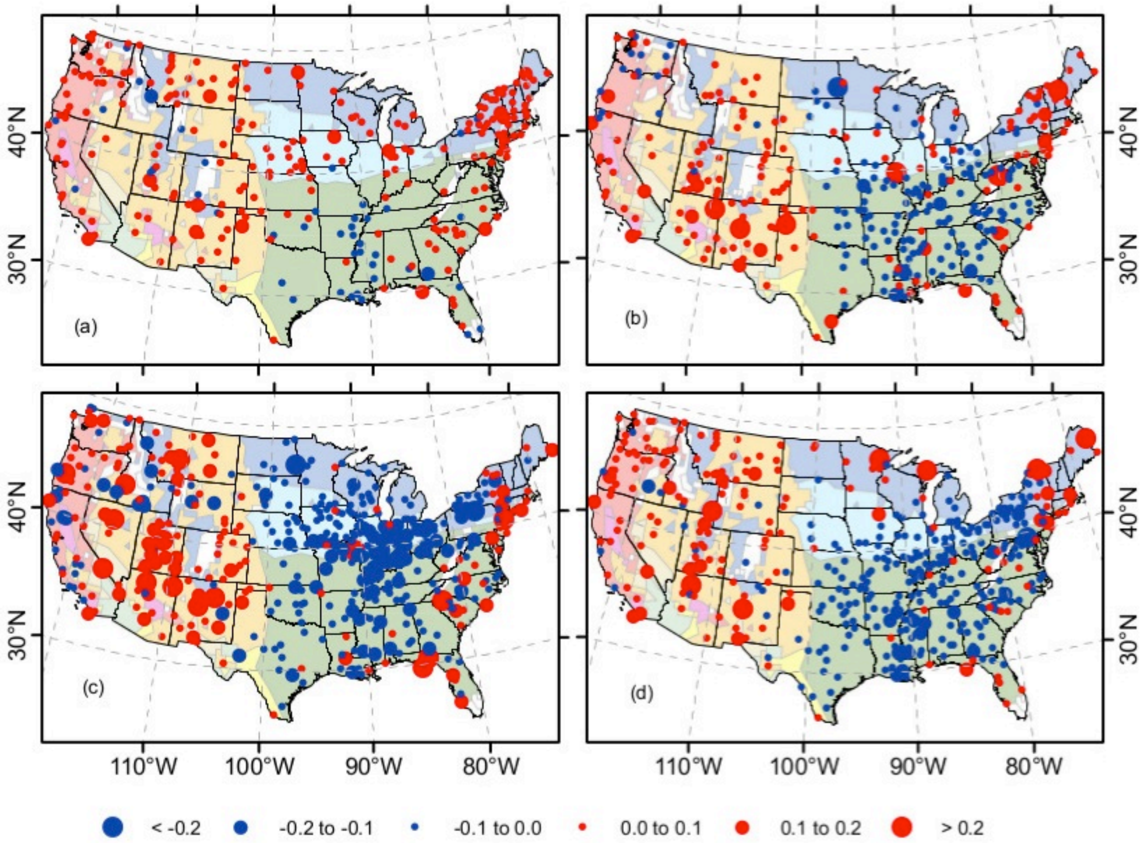

Figure 5. Slope of extreme maximum temperature events [number of extremes/year]. (a) Winter (206 significant stations), (b) Spring 263 significant stations), (c) Summer (376 significant stations) and (d) Fall (362 significant stations). Significant stations indicated by a Mann-Kendall p-value ≤ 0.05. Koeppen-Geiger classification are shown faded in bottom layer.

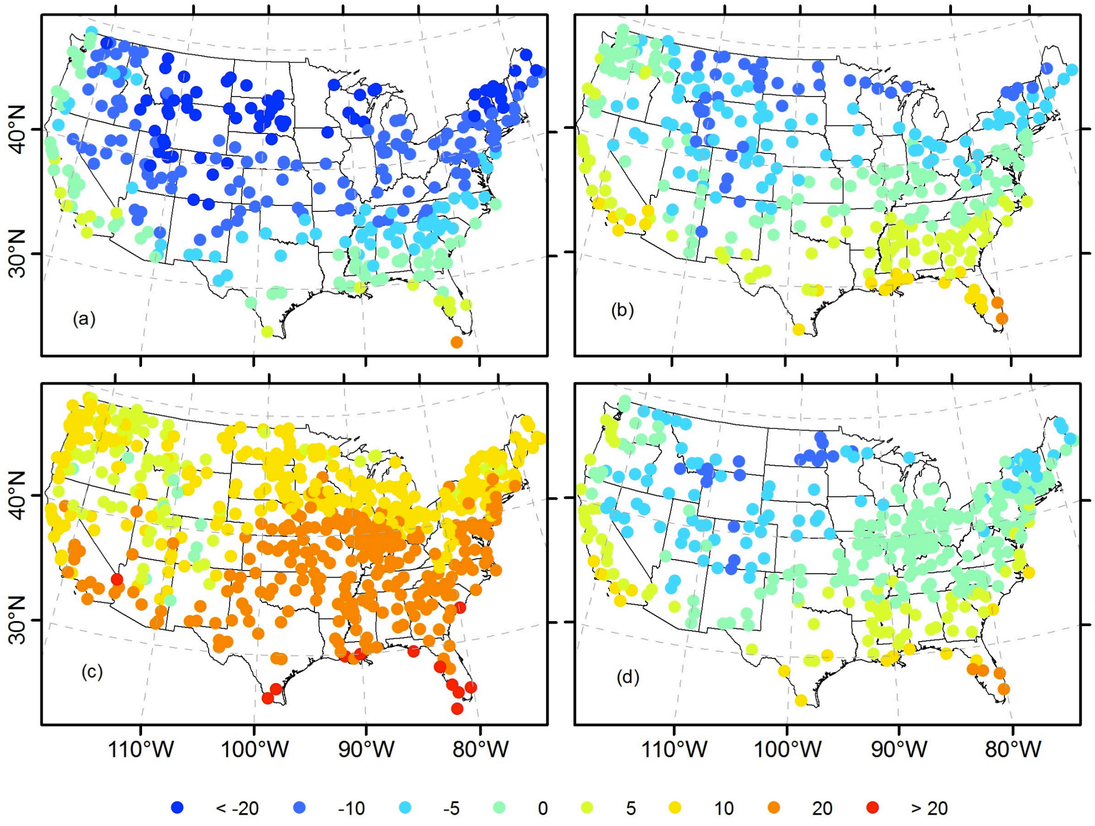

Figure 6. Magnitude threshold for an extreme minimum temperature event to occur [◦C]. (a) Winter (325 significant stations), (b) Spring (317 significant stations), (c) Summer (564 significant stations) and (d) Fall (346 significant stations). Significant stations indicated by a Mann-Kendall p-value ≤ 0.05.

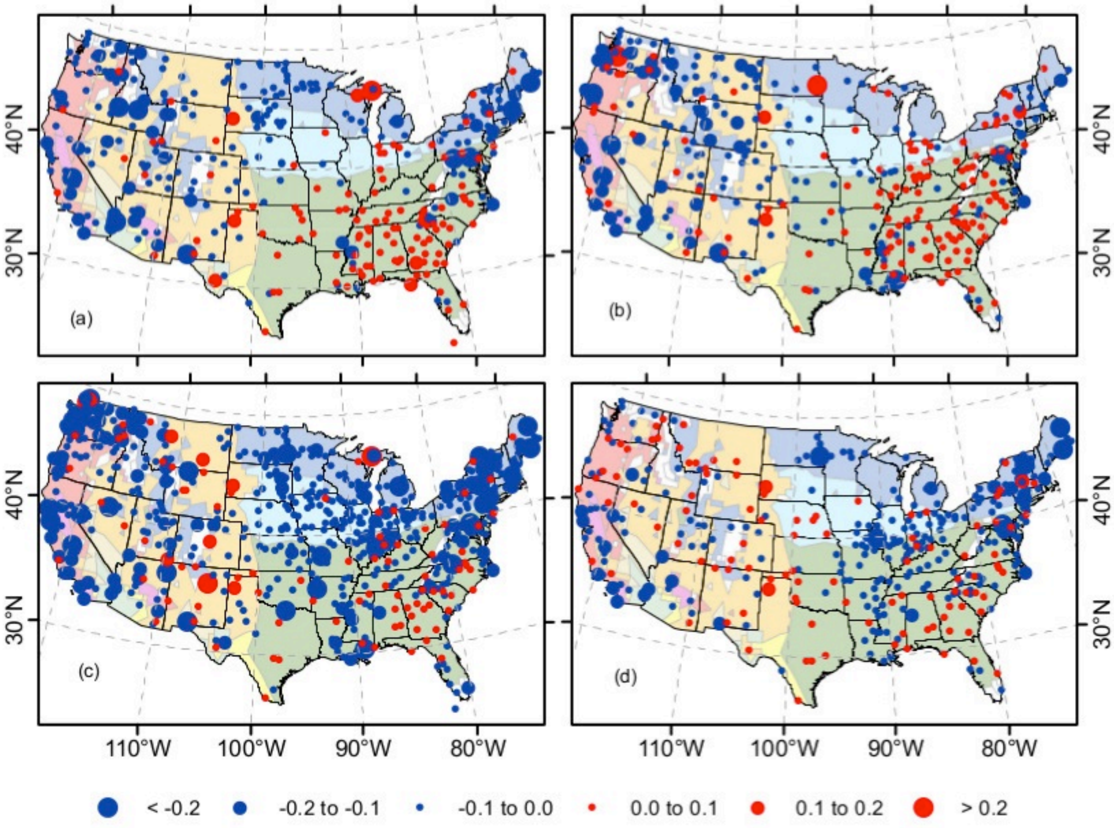

Figure 7. Slope of extreme minimum temperature events [number of extremes/year]. (a) Winter (325 significant stations), (b) Spring (317 significant stations), (c) Summer (564 significant stations) and (d) Fall (346 significant stations). Significant are stations based on the Mann-Kendall P-value ≤ 0.05. Koeppen-Geiger classification are shown faded in bottom layer.

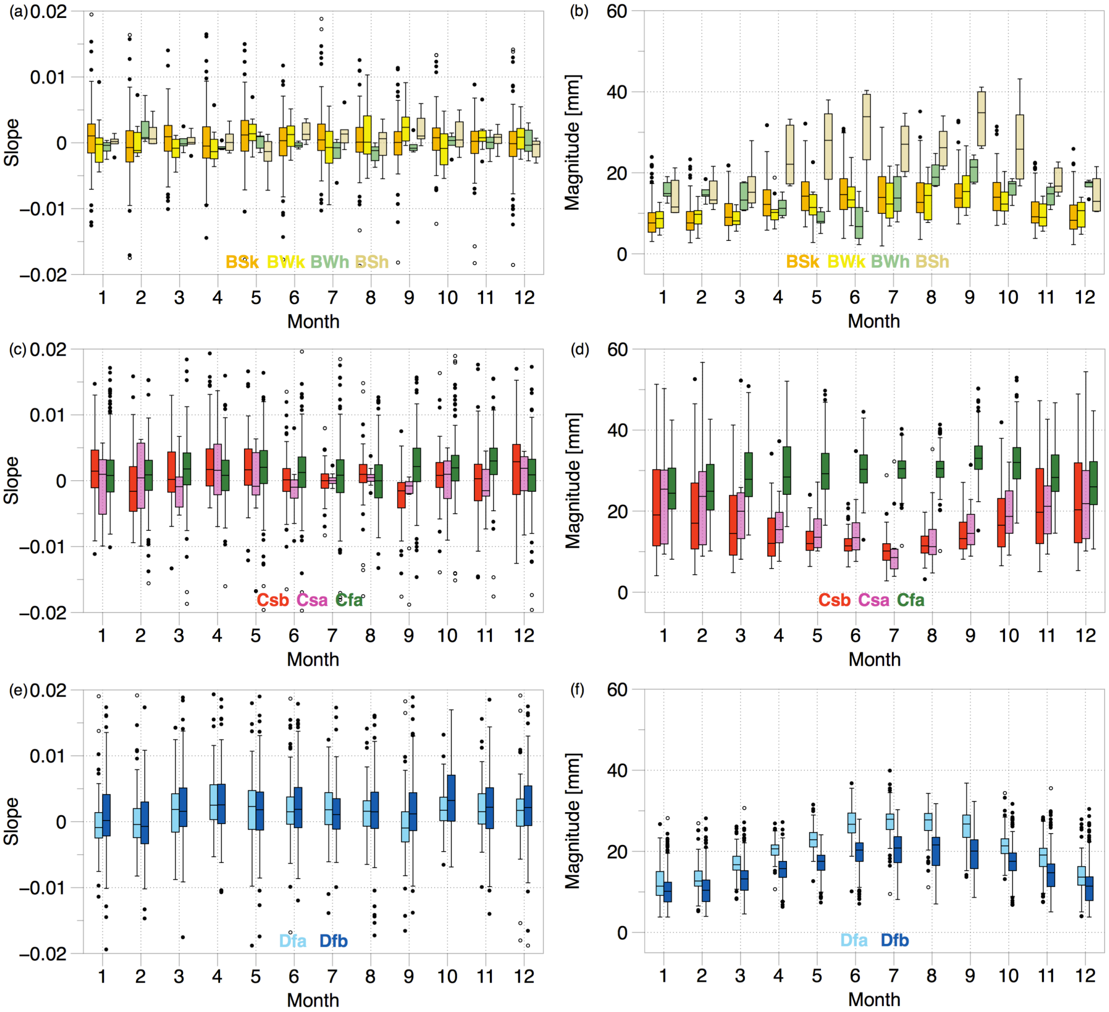

Figure 8. Mean slope [number of extremes/years of record] and magnitude [mm] values for extreme precipitation, calculated at all 958 stations. a) Slope values for Koeppen-Geiger B regions , b) Magnitude thresholds for Koeppen-Geiger B regions, c) Slope values for Koeppen-Geiger C regions, d) Magnitude thresholds for Koeppen-Geiger C regions, e) Slope values for Koeppen-Geiger D regions and f) Magnitude thresholds for Koeppen-Geiger D regions.

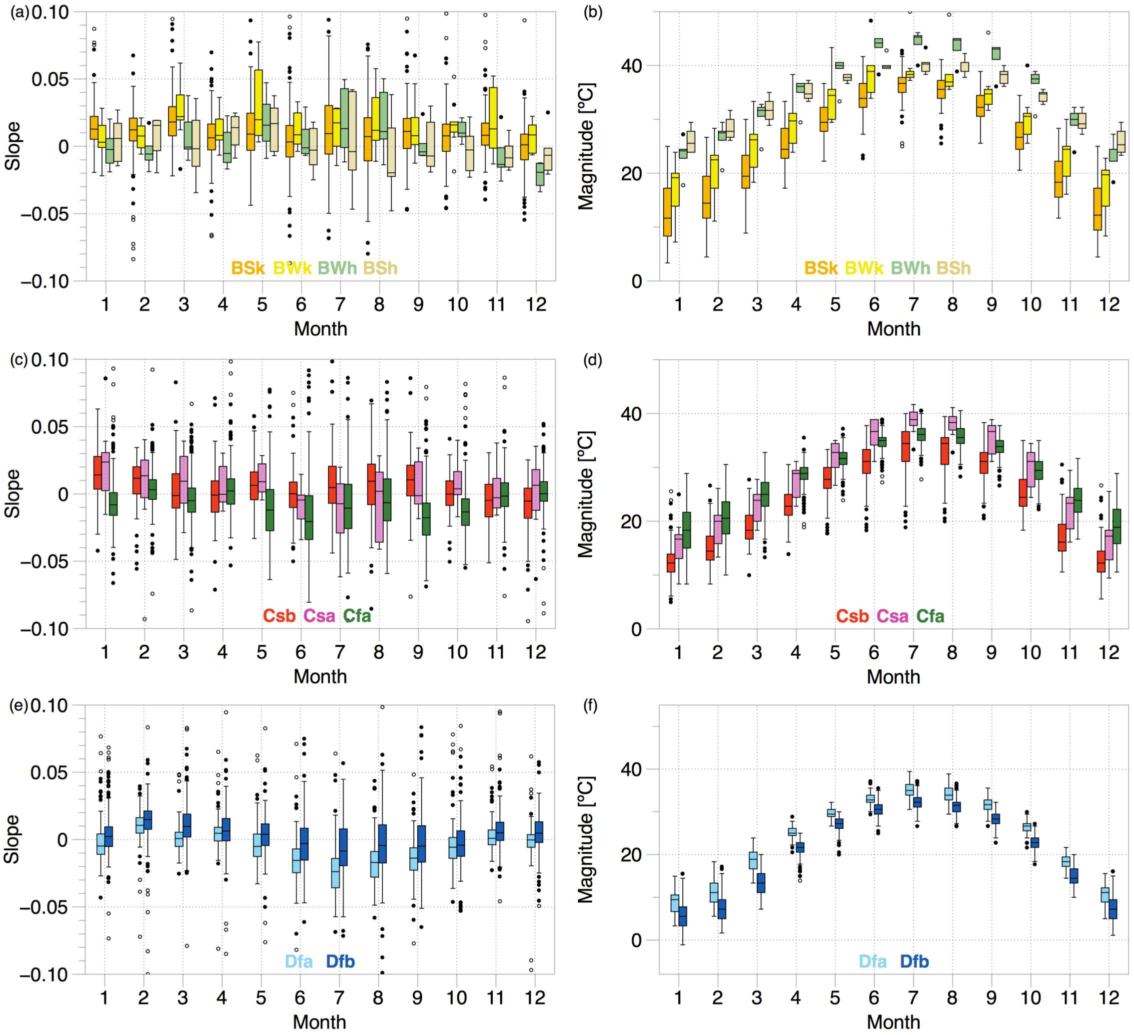

Figure 9. Mean slope [number of extremes/years of record] and magnitude [◦C] values for extreme maximum temperature, calculated at all 958 stations. a) Slope values for Koeppen- Geiger B regions, b) Magnitude thresholds for Koeppen-Geiger B regions, c) Slope values for Koeppen-Geiger C regions, d) Magnitude thresholds for Koeppen-Geiger C regions, e) Slope values for Koeppen-Geiger D regions and f) Magnitude thresholds for Koeppen-Geiger D regions.

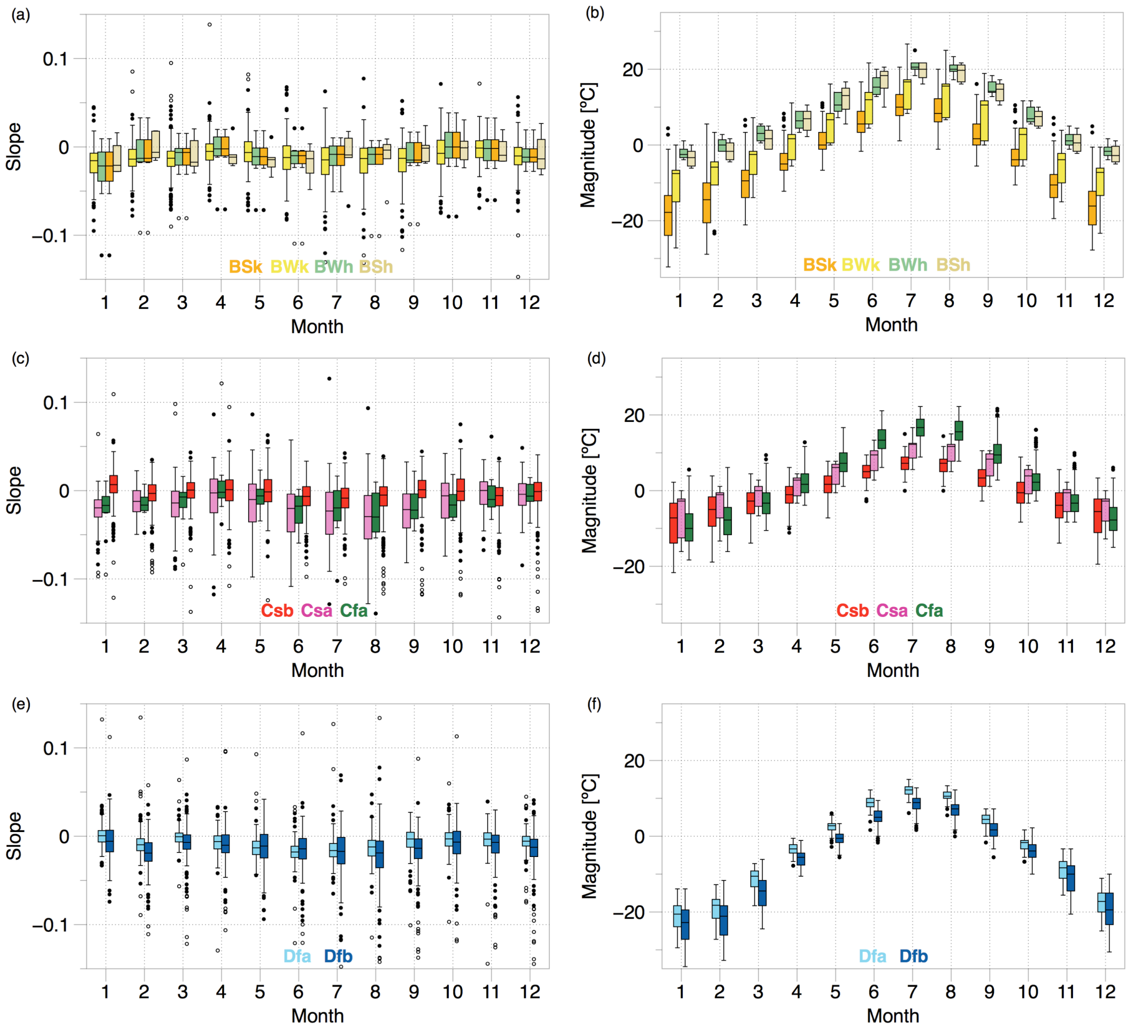

Figure 10. Mean slope [number of extremes/years of record] and magnitude [◦C] values for extreme minimum temperature, calculated at all 958 stations. a) Slope values for Koeppen- Geiger B regions, b) Magnitude thresholds for Koeppen-Geiger B regions, c) Slope values for Koeppen-Geiger C regions, d) Magnitude thresholds for Koeppen-Geiger C regions, e) Slope values for Koeppen-Geiger D regions and f) Magnitude thresholds for Koeppen-Geiger D regions.

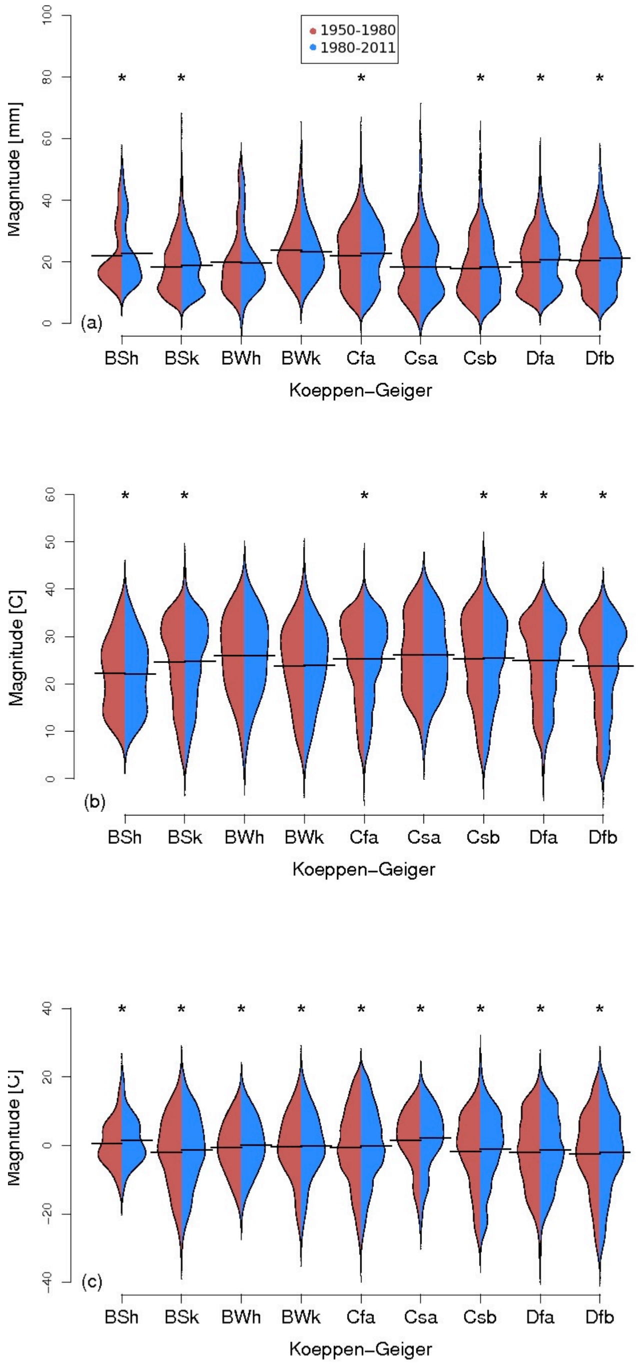

Figure 11. Two-sided bean plots comparing 1950-1980 and 1980-2011 monthly extreme magnitude thresholds. All 958 stations are represented and separated by Koeppen-Geiger region. (a) Extreme precipitation threshold [mm], (b) Extreme maximum temperature threshold [◦C], (c) Extreme minimum temperature threshold [◦C]. The asterisk (*) indicates that there is a statistical difference between the two sampled groups, significant at the 95th percentile.

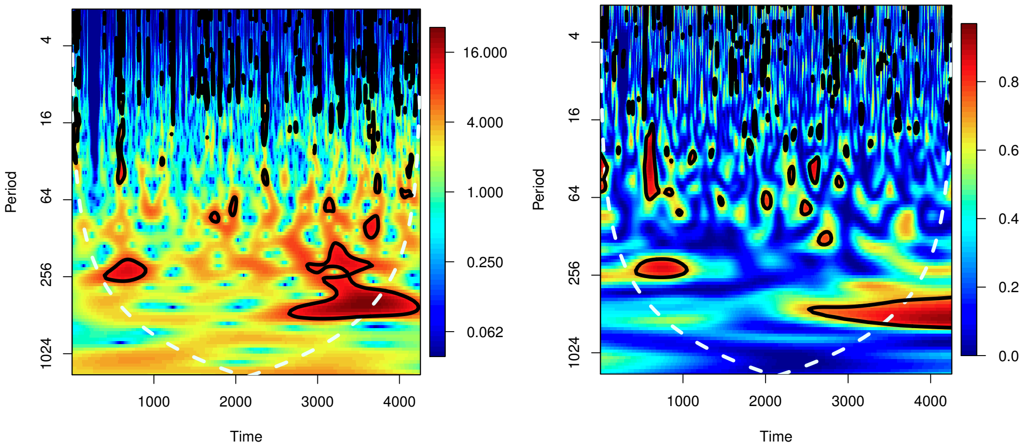

Figure 14. Results for Lawrence, KS precipitation and SOI behavior (a) Wavelet Cospectra and (b) Wavelet Coherence.

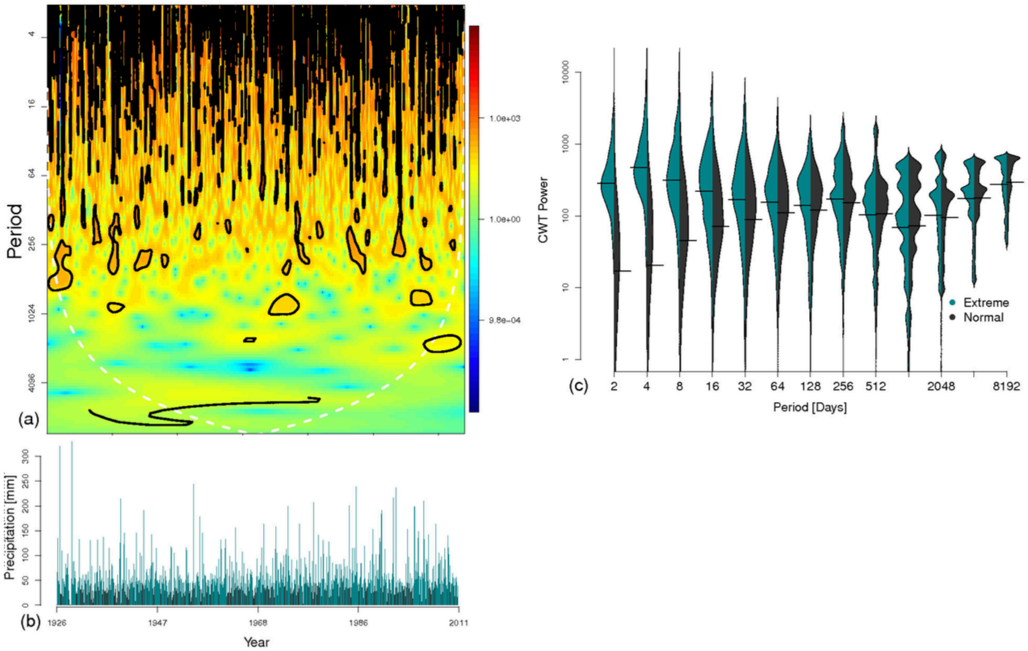

Figure 15 Results for Brewton, AL (USHCN Station 011084) daily precipi- tation continuous wavelet transform (cwt) (a), precipitation time series with extreme event highlighted (b) and bean plots representing the pdf of extreme or normal events at each timescale (c).

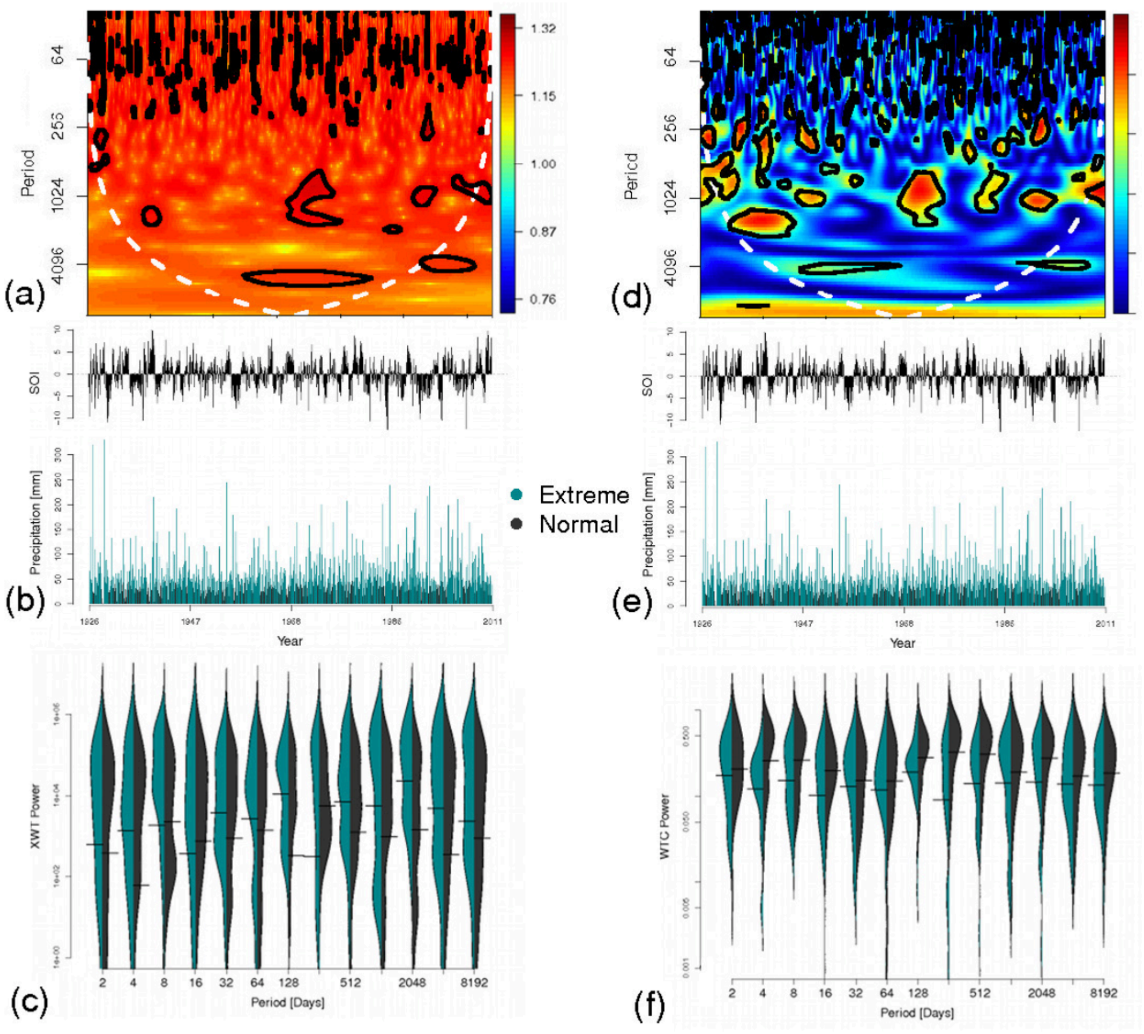

Figure 16 Results for Brewton, AL (USHCN Station 011084) daily precipitation and SOI behavior (a) cross wavelet transform (xwt), (b) the observed precipitation trend with the extremes highlighted alongside the observed SOI trend and (c) illustrating the power distribution of extreme and normal events for each period. The wtc example results are shown the following column (d) the wavelet coherence transform, (e) the observed precipitation and SOI and (f) the power distribution of the extreme and normal events throughout time.

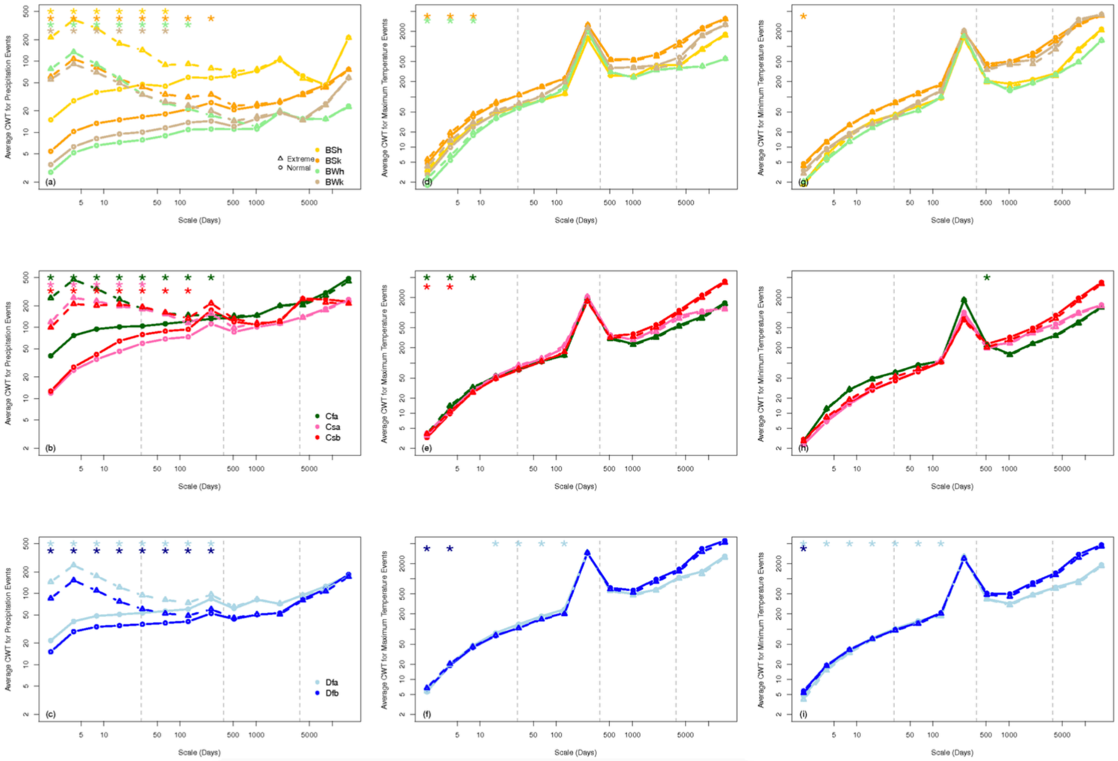

Figure 17 Continuous wavelet transform (cwt) results for precipitation (a- c), maximum temperature (d-f) and minimum temperature (g-i). Extreme (dashed) and normal (solid) results averaged across each Koeppen-Geiger region, where the arid zone is row 1, warm temperate zone is row 2 and snow zone is row 3. Vertical dashed grey lines are indicative of monthly, annual and decadal timescales respectively.

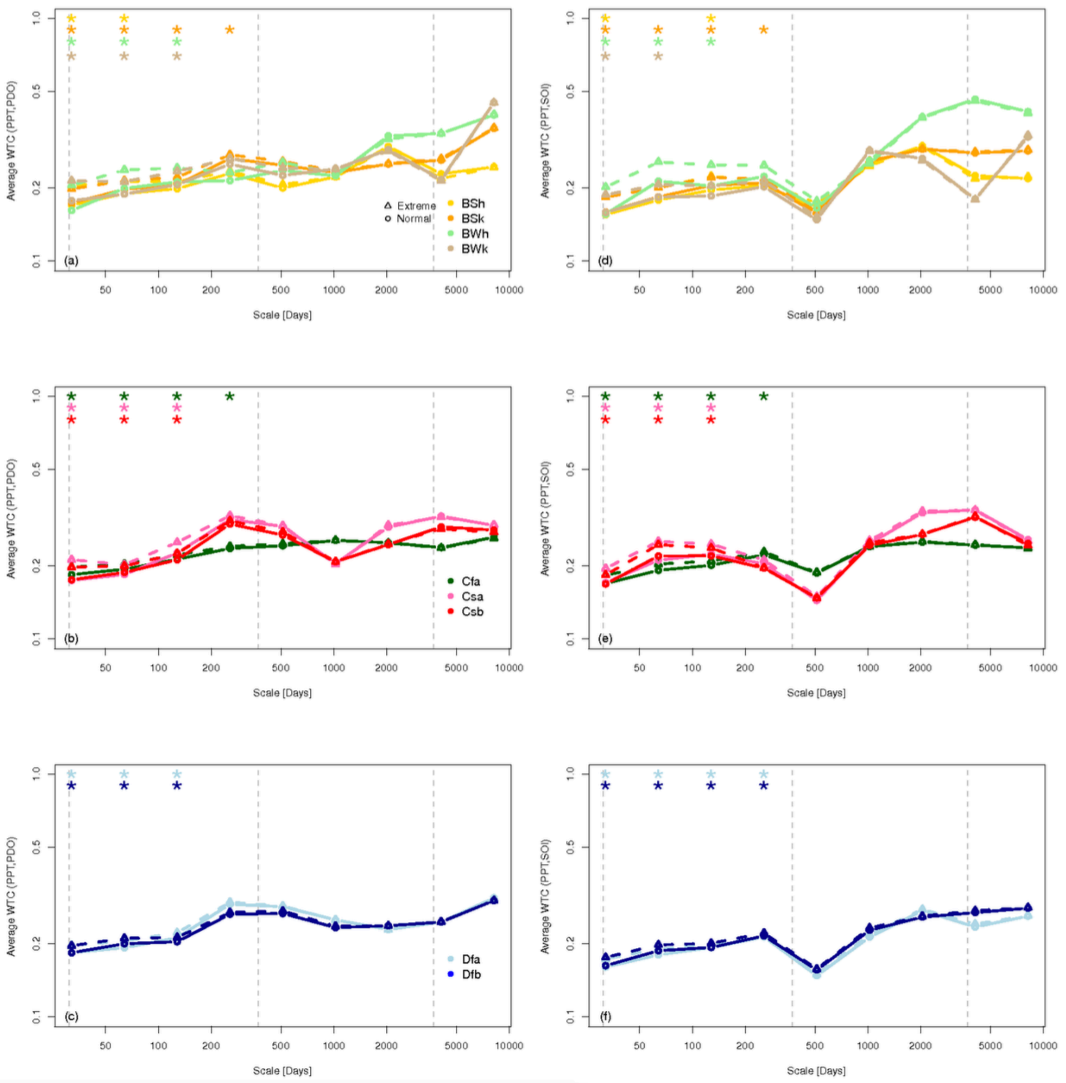

Figure 18 Wavelet coherence transform (wtc) results of precipitation and teleconnections. Extreme (dashed) and normal (solid) results averaged across each Koeppen-Geiger region, where the arid zone is row 1, warm temperate zone is row 2 and snow zone is row 3. Vertical dashed grey lines are indicative of monthly, annual and decadal timescales respectively.

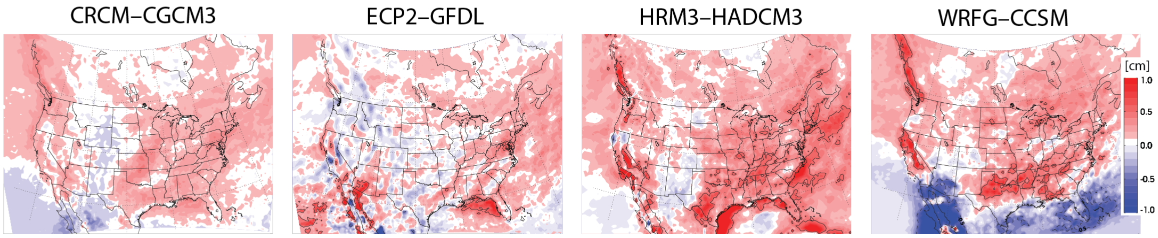

Figure 19. Differences between 21st- and 20th-century daily precipitation extremes (95th-percentile) for four different NARCCAP RCM–GCM combinations.

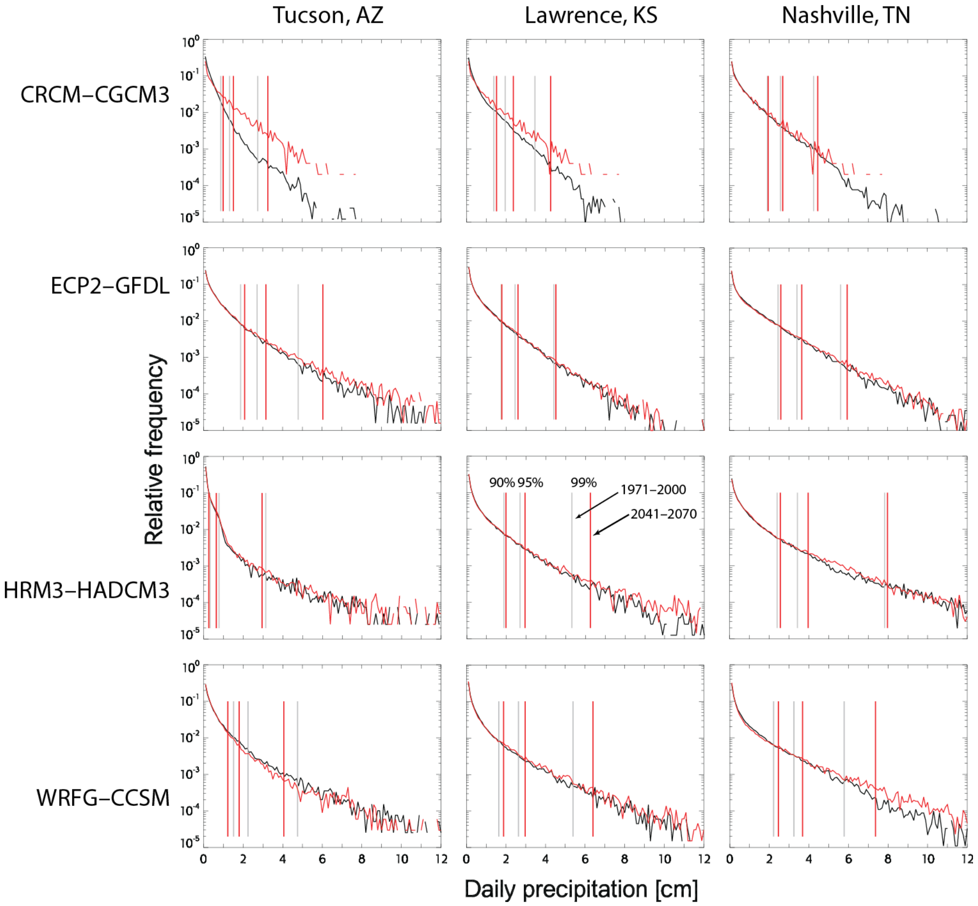

Figure 20. Distributions of daily precipitation in the vicinity of three cities for the 20th- (black) and 21st-century (red) NARCCAP simulations. Gray and red vertical lines denote 90th, 95th, and 99th percentiles.

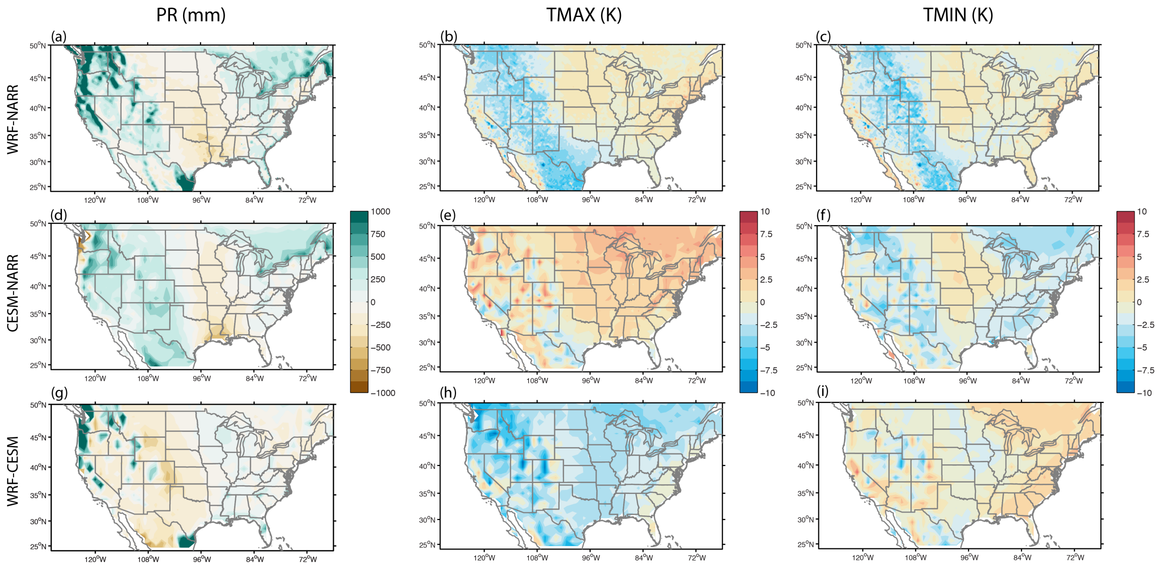

Figure 21. Quantification of GCM and RCM bias. (a), (b), and (c) show differences between WRF and NARR (WRF minus NARR); (d), (e), and (f) show differences between CESM and NARR (CESM minus NARR); (g), (h), and (i) show differences between WRF and CESM (WRF minus CESM).

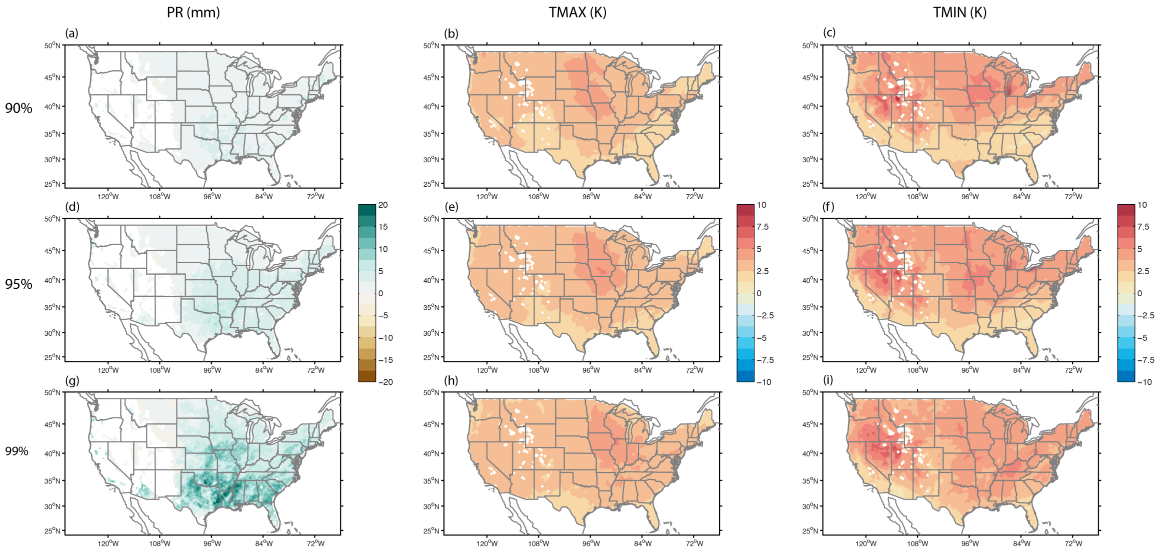

Figure 22: Differences between projected and historical extreme values corresponding to the 90th, 95th, and 99th percentile of distribution for PR (left panel), and TMAX (middle panel), and to the 1st, 5th, and 10th percentile of the distribution for TMIN (right panel).

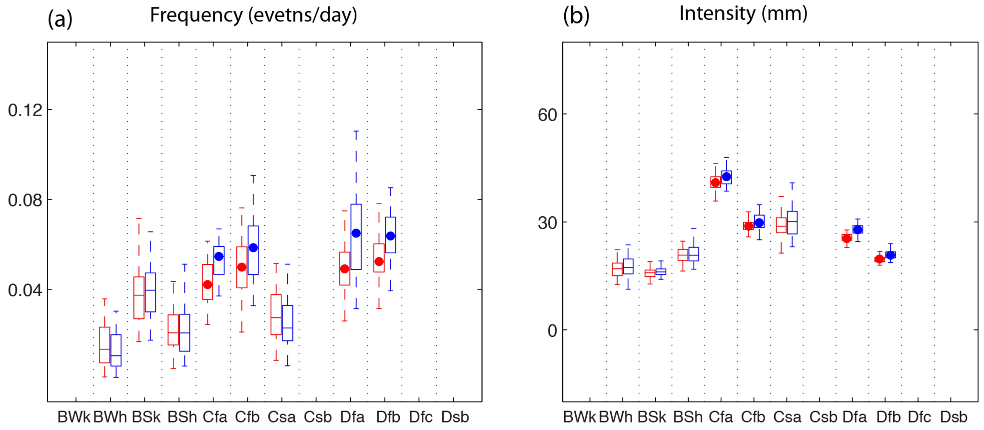

Figure 23: Box plots for frequency (a) and intensity (b) of extreme precipitation during spring. Within each climate zone, the red box denotes the historical simulation and the blue box denotes the projected simulation. Colored dots indicate the difference between the two samples in that climate zone is statistically significant.

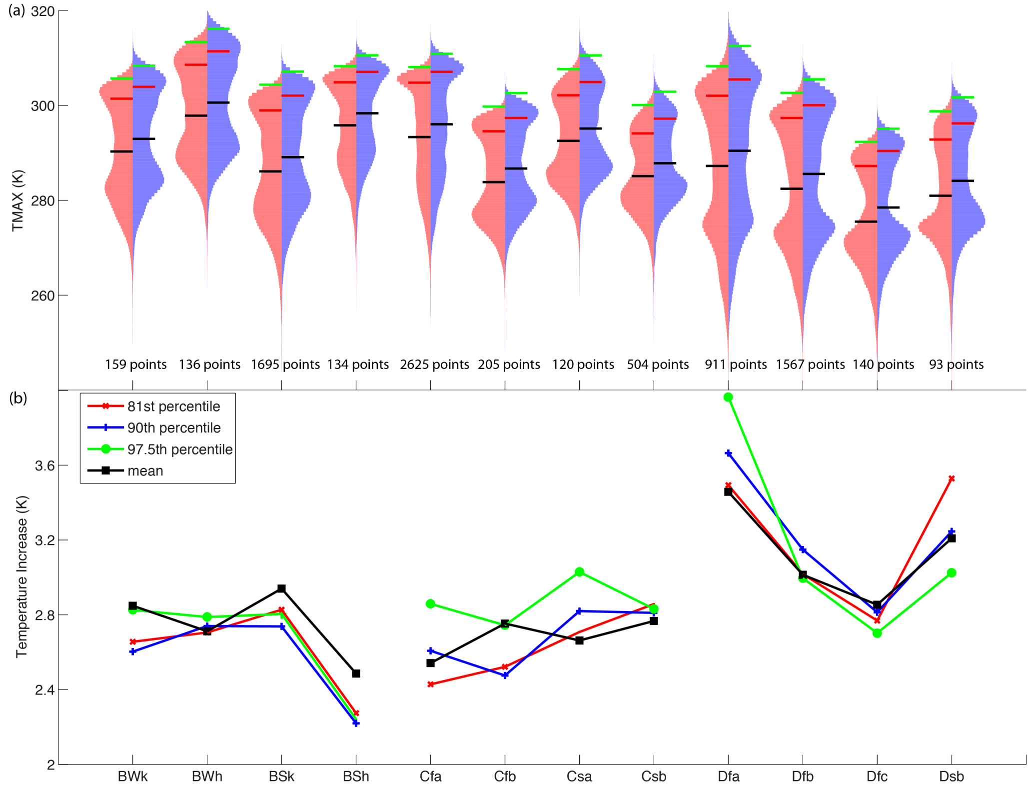

Figure 24. (a): Violin plots of the TMAX distributions for each climate zone in both the historical (red) and projected (blue) simulations. (b): TMAX increases in the projected simulation compared to the historical simulation for the 81^{st} (red), 90^{th} (blue), and 97.5^{th} (green) percentile values, as well as the mean (black) for each climate zones.

Project Participants:

Faculty:
Dr. Nathaniel Brunsell, KU
Dr. David Mechem, KU
Dr. Chungsheng Ma, WSU

Graduate Students:
Cassandra Wilson, Graduate Student KU
Lei Cai, Graduate Student KU
Qi Li, Graduate Student WSU

Joshua McCrary, Graduate Student WSU
Maryssa Metheny, Graduate Student WSU

Undergraduate Student:
Nicholas Ma, Undergraduate Student WSU

Publications

Wilson, C. J., N. A. Brunsell, L. Miller, C. B. Young and D. B. Mechem (2015). Changes in extreme weather events over the United States from 1900-2009. Climate, in review.

Ma, C. (2015). Isotropic covariance matrix functions on all spheres. Mathematical Geosciences, to appear, online version: DOI 10.1007/s11004-014-9566-6

Balakrishnan, N., Ma, C., and Wang, R. (2015). Logistic vector random fields with logistic direct and cross covariances. Journal of Statistical Planning and Inference, To appear, online version: http://dx.doi.org/10.1016/j.jspi.2015.01.004

Huber, D. B., D. B. Mechem, and N. A. Brunsell (2014). Effects of Great Plains irrigation on regional climate. Climate, **2**, 103–128.

Wang, R., Du, J., and Ma, C. (2014). Covariance matrix functions of isotropic vector random fields. Communications in Statistics - Theory and Methods, vol. 43, 2081-2093.

Ma, C. (2013). The Schoenberg-Levy kernel and relationships among fractional Brownian motion, bifractional Brownian motion, and others. Theory of Probability and Its Applications, vol.57, 619-632.

Ma, C. (2013). Student's t vector random fields with power-law and log-law decaying direct and cross covariances. Stochastic Analysis and Applications, vol. 31, 167-182.

Ma, C. (2013). Mittag-Leffler vector random fields with Mittag-Leffler direct and cross covariances. Annals of the Institute of Statistical Mathematics, vol. 65, 941-958.

Ma, C. (2013). K-distributed vector random fields in space and time. Statistics and Probability Letters, vol. 83, 1143-1150.

Du, J. and Ma, C. (2013). Vector random fields with compactly supported covariance matrix functions. Journal of Statistical Planning and Inference, vol. 143, 457-467.

Du, J., Ma, C., Li, Y. (2013). Isotropic variogram matrix functions on spheres. Mathematical Geosciences, vol. 45, 341-357.

Ma, C. (2012). Stationary and isotropic vector random fields on spheres. Mathematical Geosciences, vol. 44, 765-778 (2012 best paper award of Mathematical Geosciences).

Du, J. and Ma, C. (2012). Variogram matrix functions for vector random fields with second-order increments. Mathematical Geosciences, vol. 44, 411-425.

Du, J., Leonenko, N., Ma, C., and Shu, H. (2012). Hyperbolic vector random fields with hyperbolic direct and cross covariance functions. Stochastic Analysis and Applications, vol. 30, 662-674.

Ma, C. (2011). Vector random fields with second-order moments or second-order increments. Stochastic Analysis and Applications, vol. 29, 197-215.

Ma, C. (2011). Covariance matrix functions of vector chi-square random fields in space and time. IEEE Transactions on Communications, vol. 59, 2554-2561.

Ma, C. (2011). Vector random fields with long range dependence. Fractals, vol. 19, 249-258.

Ma, C. (2011). Covariance matrices for second-order vector random fields in space and time. IEEE Transactions on Signal Processing, vol. 59, 2160-2168.

Ma, C. (2011). A class of variogram matrices for vector random fields with second-order increments. Mathematical Geosciences, vol. 43, 229-242.

Du, J. and Ma, C. (2011). Spherically invariant vector random fields in space and time. IEEE Transactions on Signal Processing, vol. 59, 5921-5929.

Ma, C. (2010). Elliptically contoured random fields in space and time. Journal of Physics A: Mathematical and Theoretical, vol. 43, 165209 (14pp).

Ma, C. (2010) random fields in space and time. IEEE Transactions on Signal Processing, vol. 58, 378-383.

Shu, H., Ma, X. and Ma, C. (2010). Isotropic random fields with the von-Karman-Whittle type correlation structure. Communications in Statistics , Theory and Methods, vol. 39, 3504-3512.

Presentations

Cai, L., D. B. Mechem, and N. A. Brunsell, 2014: Extreme events over the continuous United States portrayed in a CESM1–WRF dynamical downscaling framework, Preprints, 26th Conference on Climate Variability and Change, Atlanta, GA, Amer. Meteor. Soc., 108.

Wilson, C., N. A. Brunsell, C. B. Young and L. Miller: 2012, Variation in 20th Century Weather Extremes as a function of Biome. AGU Fall Meeting. 3-9 December, San Francisco, CA.

Brunsell, N. A., C. J. Wilson, and D. B. Mechem, 2011: Assessing regional scale variability in North American extreme weather events. DOE CESM PI Meeting, Washington, D. C.

Mechem, D. B., and N. A. Brunsell, 2011: Preliminary results from a regional climate modeling framework for investigating North American extremes. *Proc. American Geophysical Union Fall Meeting*, San Francisco, CA, AGU.

Wilson, C.J., Brunsell, N.A.: 2011, Assessing the geographical and climate space distribution of extreme weather events. AGU Fall Meeting, 4-9 Dec, San Francisco, California.

Wilson, C.J., Brunsell, N.A.: 2011, Understanding the spatial variation in timescales of extreme precipitation across the United States. WCRP Open Science Conference, 24-28 Oct, Denver, Colorado.

Wilson, C.J., Brunsell, N.A.: 2012, Assessing the geographical and climate space distribution of extreme weather events. Graduate Research Competition, 7 Mar, Lawrence, Kansas.

Wilson, C.J., Brunsell, N.A.: 2012, Assessing the geographical and climate space distribution of extreme weather events. Kansas EPSCoR Meeting, 8 Jan, Manhattan, Kansas.

Du, J., Ma, C. and Demel, S. S.: 2012 Compactly supported covariance matrix models with application to spatial tapering, American Mathematical Society 2012 Spring Central Section Meeting #1081, March 30 - April 1, 2012, Department of Mathematics, University of Kansas, Lawrence, Kansas

Metheny, M.: 2012, Multiple time series with long memory, Seminar on Stochastic Processes 2012, March 22-24, 2012, Department of Mathematics, University of Kansas, Lawrence, Kansas.

Metheny, M. and Ma, N.: 2012, Analysis of Kansas temperature: 1893-2009, Kansas: Climate Change and Energy Central, 2012 Statewide EPSCoR Conference, January 12-13, 2012, Wichita, Kansas.

Metheny, M. and Ma, N.: 2012, Analysis of Kansas temperature: 1893-2009, Climate and Agriculture: Meeting the Needs for Kansas, Kansas NSF EPSCoR Annual Meeting and Site Review, January 8-10, 2012, Kansas State University Alumni Center, Manhattan, Kansas.

Ma, C., 2011, Logistic vector random fields with logistic direct and cross covariances, International Conference on Advances in Probability and Statistics - Theory and Applications: A Celebration of N. Balakrishnan's 30 years of Contributions to Statistics, Dec. 28 - 31, Hong Kong, China.

Du, J. and Ma, C., 2011: Compactly supported multivariate covariance matrix functions, 2011 Joint Statistical Meetings, Miami Beach, Florida, July 30 - August 4, 2011.

Ma, C., 2011: Extreme data analysis of Kansas temperature data, ESF-COST High-Level Research Conference on Extreme Environmental Events, Cambridge, UK, Dec. 13-17, 2010